

Oscillatory two- and three-dimensional thermocapillary convection

By JIEYONG XU AND ABDELFATTAH ZEBIB

Department of Mechanical and Aerospace Engineering, Rutgers University,
Piscataway, NJ 08854-8058, USA

(Received 3 July 1997 and in revised form 20 January 1998)

The character and stability of two- and three-dimensional thermocapillary driven convection are investigated by numerical simulations. In two dimensions, Hopf bifurcation neutral curves are delineated for fluids with Prandtl numbers (Pr) 10.0, 6.78, 4.4 and 1.0 in the Reynolds number (Re)–cavity aspect ratio (A_x) plane corresponding to $Re \leq 1.3 \times 10^4$ and $A_x \leq 7.0$. It is found that time-dependent motion is only possible if A_x exceeds a critical value, A_{xcr} , which increases with decreasing Pr . There are two coexisting neutral curves for $Pr \geq 4.4$. Streamline and isotherm patterns are presented at different Re and A_x corresponding to stationary and oscillatory states. Energy analyses of oscillatory flows are performed in the neighbourhood of critical points to determine the mechanisms leading to instability. Results are provided for flows near both critical points of the first unstable region with $A_x = 3.0$ and $Pr = 10$.

In three dimensions, attention is focused on the influence of sidewalls, located at $y = 0$ and $y = A_y$, and spanwise motion on the transition. In general, sidewalls have a damping effect on oscillations and hence increase the magnitude of the first critical Re . However, the existence of spanwise waves can reduce this critical Re . At large aspect ratios $A_x = A_y = 15$, our results with $Pr = 13.9$ at the lower critical Reynolds number of the first unstable region are in good agreement with those from infinite layer linear stability analysis.

1. Introduction

Understanding fluid motion is important in material processing technologies. In crystal growth from the melt, single crystals with uniform material properties are desired, but homogeneity in crystals can be destroyed if melt motion is unsteady (Hurle 1967; Müller 1988). In the terrestrial environment, buoyancy and thermocapillarity are two major causes for convection. However, in a low-gravity environment, thermocapillary convection becomes dominant.

Thermocapillary flows have received considerable attention in the past few decades. Levich & Krylov (1969), Ostrach (1982) and Davis (1987) provide reviews. Early theoretical articles can be found in Birikh (1966) and Yih (1968). A rich body of two-dimensional numerical investigations is also available in the literature. Zebib, Homsy & Meiburg (1985) investigated high Marangoni number thermocapillary convection in a square cavity and confirmed the scaling analysis in Ostrach (1982) for the boundary layer regime. Carpenter & Homsy (1990) further examined the Prandtl number dependence, as well as structure and stability of this flow. Their results showed no evidence

of unsteady behaviour for Ma up to $O(10^5)$. Strani, Piva & Graziani (1982) and Wilke & Löser (1983) provided results for thermocapillary convection in rectangular cavities with aspect ratios other than one. Ben Hadid & Roux (1990) also considered the case of fluid with small Prandtl number, $Pr = 0.015$, in cavities of various A_x without discovering any oscillatory flow field. Results of numerical simulation of oscillatory thermocapillary convection of a fluid with moderate $Pr = 6.78$ were reported by Peltier & Biringen (1993). They provided a stability diagram in the (A_x, Ma) -plane, and found a minimum critical A_x near 2.3 and a minimum critical Ma near 20 000 within the range $A_x \leq 3.8$.

While most of the numerical investigations of thermocapillary convection considered two-dimensional situations, recent three-dimensional investigations can be found in Saß, Kuhlmann & Rath (1996) which considered steady three-dimensional thermocapillary convection in a cubic container, and in Levenstam & Amberg (1995) which investigated hydrodynamical instabilities of thermocapillary flow in a half-zone.

Discussions of instability mechanisms can be found in Smith & Davis (1983, referred to as SD in this paper), and Smith (1986) for dynamic thermocapillary infinite liquid layers, and in Wanschura *et al.* (1995) for thermocapillary liquid bridges. Peltier & Biringen (1993) also provided some description of the oscillatory instability relating the temporal evolution of large-scale structures in the flow and their interaction with the temperature sensitive free surface.

Numerous experiments (Chun & Wuest 1979; Chun 1980; Preisser, Schwabe & Scharmann 1983; Kamotani, Ostrach & Vargas 1984 and Velten, Schwabe & Scharmann 1991) have demonstrated the existence of thermocapillary instabilities, i.e. when the Marangoni number (Ma) exceeds a critical value, the motion undergoes a transition from steady to oscillatory flow.

More recent experiments by Daviaud & Vince (1993), De Saedeleer, Garcimartin & Platten (1996), Riley & Neitzel (1996), and Braunfurth & Homsy (personal communication 1996, 1997) examined various two-dimensional and three-dimensional transitions, in pure thermocapillary flow or when combined with buoyancy-driven flows, in layers and cavities. Typically, moderate- Pr fluids are used in these experiments (10, 15, 13.9 and 4.4, respectively).

In the present study, we report on reasonably complete investigations of oscillatory thermocapillary convection in rectangular cavities. In two dimensions, the influence of Pr , Re , and A_x on the motion is studied. An energy analysis is performed to assess various contributions to fluctuating quantities, and hence gain insight into the origin of and identify the mechanism responsible for transition. In three dimensions, because of high computing costs, we only consider $Pr = 4.4$ and 13.9 since experimental results are available with these fluids. We investigate what would happen if a thermocapillary flow in a cavity with $A_x = 3$ is allowed to become three-dimensional. The dual effects of sidewalls which should have a damping effect, and the simultaneous possibility of a spanwise instability turn out to be Pr -dependent. When $Pr = 4.4$, we find that coexistence of spanwise and streamwise fluctuations destabilizes the flow at Re lower than that required to trigger a pure two-dimensional streamwise instability at the same A_x . With $Pr = 13.9$, sidewalls continue to exhibit their damping effect even with A_y as large as 20, while spanwise fluctuations are much weaker than streamwise fluctuations when Re is near its first critical value. We also consider a case resembling an infinite layer with $A_x = A_y = 15$. Reasonable agreement with the wave motion of SD is demonstrated.

2. Physical and mathematical models

2.1. Physical model for the two- and three-dimensional thermocapillary convection

Thermocapillary convection of an incompressible, Newtonian fluid is considered. In two dimensions, the flow is in a rectangular cavity with height H and length $A_x \times H$ (A_x is the length aspect ratio). Two vertical isothermal side-walls are kept at temperatures T_h on the left and T_c on the right. The bottom boundary is rigid while the top boundary is a non-deformable flat free surface open to a passive gas and also insulating. Both bottom and top boundaries are assumed to be adiabatic. In three dimensions, the front and back sidewalls are introduced to form a box with width $A_y \times H$ (A_y is the width aspect ratio). These sidewalls are also assumed to be thermally adiabatic.

Surface tension on the free surface is assumed to be a linear function of temperature as $\sigma = \sigma_0 - \gamma(T - T_0)$, in which $\gamma = -\partial\sigma/\partial T$ and subscript 0 is a reference state.

2.2. Mathematical models

2.2.1. Two-dimensional model in stream function – vorticity formulation

The non-dimensional mathematical model for the two-dimensional cavity thermo-capillary convection is described by a stream function–vorticity formulation, as

$$\nabla^2\psi = -\omega, \tag{1}$$

$$\frac{\partial\omega}{\partial\tau} + Re\nabla \cdot (\omega\mathbf{V}) = \nabla^2\omega, \tag{2}$$

$$\frac{\partial T}{\partial\tau} + Re\nabla \cdot (T\mathbf{V}) = \frac{1}{Pr}\nabla^2 T, \tag{3}$$

where

$$\mathbf{V} = (u, v) \quad \text{with} \quad u = \frac{\partial\psi}{\partial z} \quad v = -\frac{\partial\psi}{\partial x}, \tag{4}$$

with boundary conditions:

$$\left. \begin{aligned} \psi = 0, \quad \frac{\partial\psi}{\partial x} = 0 \quad T = 1 \quad \text{at } x = 0; \\ \psi = 0, \quad \frac{\partial\psi}{\partial x} = 0 \quad T = 0 \quad \text{at } x = Ax; \\ \psi = 0, \quad \frac{\partial\psi}{\partial z} = 0 \quad \frac{\partial T}{\partial z} = 0 \quad \text{at } z = 0 \\ \psi = 0, \quad \omega = \frac{\partial T}{\partial x}, \quad \frac{\partial T}{\partial z} = 0 \quad \text{at } z = 1 \end{aligned} \right\} \tag{5}$$

Here length, temperature, velocity and time are assumed dimensionless with respect to H , $\Delta T = (T_h - T_c)$, $\gamma\Delta T/\mu$ and H^2/ν , respectively, and

$$Pr = \frac{\nu}{\alpha}, \quad Re = \gamma \frac{\Delta TH}{\mu\nu}. \tag{6}$$

where μ , ν and α are dynamic viscosity, kinematic viscosity, and thermal diffusivity respectively.

2.2.2. Three-dimensional model in primitive variables

The dimensionless mathematical three-dimensional model of convection in a rectangular cavity ($A_x \times A_y \times 1$) is

$$\nabla \cdot \mathbf{V} = 0, \quad (7)$$

$$\frac{\partial \mathbf{V}}{\partial \tau} + Re \nabla \cdot (\mathbf{V} \mathbf{V}) = -\nabla P + \nabla^2 \mathbf{V}, \quad (8)$$

$$\frac{\partial T}{\partial \tau} + Re \nabla \cdot (T \mathbf{V}) = \frac{1}{Pr} \nabla^2 T, \quad (9)$$

where

$$\mathbf{V} = (u, v, w) \quad (10)$$

with boundary conditions:

$$u = v = w = 0 \quad \text{on } x = 0, A_x \quad \text{and } y = 0, A_y \quad \text{and } z = 0 \quad (11)$$

and

$$\frac{\partial u}{\partial z} = -\frac{\partial T}{\partial x}, \quad \frac{\partial v}{\partial z} = -\frac{\partial T}{\partial y}, \quad v = 0, \quad \text{on } z = 1. \quad (12)$$

All walls are considered adiabatic, except that

$$T = 1 \quad \text{on } x = 0, \quad T = 0 \quad \text{on } x = A_x. \quad (13)$$

2.2.3. Reynolds–Orr equation for two-dimensional energy analysis

To gain insight into the instability mechanisms involved, we perform an energy analysis for flows with Re in the neighbourhoods of different critical points. The oscillatory flow is decomposed into its mean and fluctuating components as

$$T = T_0 + t, \quad P = P_0 + p, \quad U = U_0 + u, \quad V = V_0 + v, \quad (14)$$

in which the pressure P is obtained by solving a Poisson equation after we compute the velocity field.

Starting from the momentum equations in primitive variables and introducing the fluctuation kinetic energy as $k = \frac{1}{2}(u^2 + v^2)$, we derive the rate of change of k as

$$\begin{aligned} \frac{Dk}{D\tau} = & -Re \left[uu \frac{\partial U_0}{\partial x} + vv \frac{\partial V_0}{\partial y} + uw \left(\frac{\partial U_0}{\partial y} + \frac{\partial V_0}{\partial x} \right) \right] \\ & -u \frac{\partial p}{\partial x} - v \frac{\partial p}{\partial y} + \nabla^2 k - \left(\frac{\partial u}{\partial x} \right)^2 - \left(\frac{\partial u}{\partial y} \right)^2 - \left(\frac{\partial v}{\partial x} \right)^2 - \left(\frac{\partial v}{\partial y} \right)^2. \end{aligned} \quad (15)$$

Integrating over the whole domain and applying the Gaussian theorem, we find the rate of change of the total fluctuation kinetic energy K to be

$$\frac{dK}{d\tau} = \frac{d}{d\tau} \left(\int_{\Omega} k d\Omega \right) = I_{k_1} + I_{k_2} + I_{k_3}, \quad (16)$$

where

$$I_{k_1} = -Re \int_{\Omega} \left[uu \frac{\partial U_0}{\partial x} + vv \frac{\partial V_0}{\partial y} + uw \left(\frac{\partial U_0}{\partial y} + \frac{\partial V_0}{\partial x} \right) \right] d\Omega, \quad (17)$$

$$I_{k_2} = \int_{\Omega} (\nabla^2 k) d\Omega = \int_{\Gamma} u \frac{\partial u}{\partial y} d\Gamma, \quad (18)$$

$$I_{k_3} = - \int_{\Omega} \left[\left(\frac{\partial u}{\partial x} \right)^2 + \left(\frac{\partial u}{\partial y} \right)^2 + \left(\frac{\partial v}{\partial x} \right)^2 + \left(\frac{\partial v}{\partial y} \right)^2 \right] d\Omega, \quad (19)$$

with I_{k_1} , I_{k_2} and I_{k_3} denoting kinetic energy production, diffusion (also representing the rate of work done by thermocapillary stresses), and dissipation, respectively.

Similarly, defining $\theta = \frac{1}{2}t^2$ as the fluctuation thermal energy, we find the rate of change of θ to be

$$\frac{D\theta}{D\tau} = -Re \left(tu \frac{\partial T_0}{\partial x} + tv \frac{\partial T_0}{\partial y} \right) + \frac{1}{Pr} \left[\nabla^2 \theta - \left(\frac{\partial t}{\partial x} \right)^2 - \left(\frac{\partial t}{\partial y} \right)^2 \right], \quad (20)$$

and the rate of change of the total fluctuation thermal energy Θ to be

$$\frac{d\Theta}{d\tau} = \frac{d}{d\tau} \left(\int_{\Omega} \theta d\Omega \right) = I_{t_1} + I_{t_2} \quad (21)$$

in which

$$I_{t_1} = -Re \int_{\Omega} \left(tu \frac{\partial T_0}{\partial x} + tv \frac{\partial T_0}{\partial y} \right) d\Omega, \quad (22)$$

$$I_{t_2} = -\frac{1}{Pr} \int_{\Omega} \left[\left(\frac{\partial t}{\partial x} \right)^2 + \left(\frac{\partial t}{\partial y} \right)^2 \right] d\Omega \quad (23)$$

are thermal energy production and dissipation, respectively.

3. Numerical aspects

To perform nonlinear stability analysis of thermocapillary convection through numerical simulation, both efficiency and accuracy are extremely important for the numerical solver.

3.1. The two-dimensional stream function–vorticity (ψ – ω) solver

For two-dimensional calculations in ψ – ω , the coupled system is solved by a finite-volume-based scheme, in which the Poisson equation for ψ is solved by the SOR method. Velocities are obtained as spatial derivatives of ψ . At the beginning of each time step, a second-order-accurate extrapolation scheme is used to predict ψ at the current time step from its previous values in order to obtain current velocities, and therefore linearize both vorticity transport and energy equations. These two linearized equations are then solved by the alternating direction implicit (ADI) method. All time derivatives and spatial derivatives including boundary conditions are approximated in second-order accuracy.

The ψ – ω code was also designed for outstanding performance on vector computers. For example, on the CRAY C90 at the Pittsburgh Supercomputing Center, this code runs at up to 477 Mflops.

Validation of the two-dimensional solver was carefully done by comparing our solutions with those available in the literature on a number of problems with steady and transient solutions. Details of the validation can be found in Xu (1997). Two examples of comparison are provided here.

Pr	Mesh	$Re(\times 10^{-4})$	$-\psi_{min}(\times 10^3)$	$\omega_{core}(\times 10^2)$	x_c	y_c	$u(0.5, 1)(\times 10^2)$	$Nu_{x=0}$	$Nu_{x=1}$	Note
1.0	101×101	10.0	3.21	-7.01	0.57	0.63	3.05	4.36	4.36	X&Z
	$64 \times 64N$	10.0	3.23	-6.97	0.58	0.62	2.96	4.36	4.33	C&H
	$31 \times 31N$	10.0	3.24	-7.29	N/A	N/A	3.06	4.30	4.44	P&B
30	101×101	2.0	1.69	-6.27	0.43	0.78	1.49	6.61	6.61	X&Z
	$92 \times 78N$	2.0	2.13	-7.40	N/A	N/A	1.86	6.42	6.29	C&H
	$74 \times 74N$	2.0	1.82	-6.53	N/A	N/A	1.61	7.14	6.69	P&B
50	101×101	1.0	1.40	-6.19	0.36	0.80	1.12	5.91	5.91	X&Z
	$74 \times 74N$	1.0	1.77	-7.57	N/A	N/A	1.43	5.77	5.82	C&H
	$74 \times 74N$	1.0	1.44	-6.01	N/A	N/A	1.16	6.09	5.76	P&B

TABLE 1. Thermocapillary convection in a square cavity. Note: ‘N’ after the value of mesh resolution indicates a non-uniform mesh. C&H, P&B and X&Z are Carpenter & Homsy (1989), Peltier & Biringen (1993), and the present paper, respectively.

Group	ψ_{max}	Frequency	Mesh
This work	0.627	15.5	101×41
Bottaro <i>et al.</i>	0.6370	15.30	62×32
Ohshima and Ninokata	NA	15.9	80×20
Extremet <i>et al.</i>	NA	15.7	$81 \times 31N$
Shimizu	NA	15.9	81×21
Pulicani <i>et al.</i>	0.62309	15.94	30×23
Daube & Rida	NA	15.80	105×41

TABLE 2. Natural convection at $Ra = 20000$, $Pr = 0.15$, and $A_x = 4$. Results of various researchers are in Roux (1990).

One of our test cases is steady thermocapillary convection in a square cavity. Numerical studies of this problem can be found in Carpenter & Homsy (1989) and Peltier & Biringen (1993). Comparison of results is given in table 1 for a number of combinations of Pr and Re . In the table, ψ_{min} stands for minimum stream function value, $u(0.5, 1)$ is velocity at the centre of the top free surface. $Nu_{x=0}$ and $Nu_{x=1}$ are average Nusselt numbers at $x = 0$ and $x = 1$ respectively. Excellent agreement is reached for the first case of $Pr = 1$ and $Re = 10^4$, with difference being less than 3%. Reasonably good agreement is also found in the other two cases.

The second test problem is oscillatory natural convection of the $Pr = 0.015$ fluid in an $A_x = 4.0$ rectangular cavity. This model has received extensive attention. Results from a number of groups were presented and compared at the 1989 GAMM Workshop, see Roux (1990). Comparison is given in table 2 for the case of oscillatory natural convection ($Ra = 20000$) in a cavity with an adiabatic traction free surface. Excellent agreement can be seen for the value of ψ_{ave} which is the time average of maximum stream function, and oscillation frequency of the flow field.

3.2. The three-dimensional primitive variable solver

For three-dimensional simulations, a finite-volume-based primitive variable solver was developed. After discretizing the coupled partial differential equations, a semi-implicit fractional step method is used for the time marching procedure of the momentum equations (see Xu 1997 for details of the scheme). A non-staggered

Ra	Mesh	Nu_{avg}	u_{max}	y	v_{max}	x	Group
10^4	$62 \times 62 \times 62N$	2.10	0.201	0.183	0.225	0.883	FHKF
	$24 \times 24 \times 24$	2.06	0.202	0.175	0.220	0.890	This Work
	$40 \times 40 \times 40$	2.06	0.199	0.175	0.220	0.875	This Work
10^5	$62 \times 62 \times 62N$	4.36	0.147	0.145	0.247	0.935	FHKF
	$24 \times 24 \times 24$	4.42	0.141	0.150	0.261	0.925	This Work
	$32 \times 32 \times 32$	4.37	0.142	0.150	0.252	0.932	This Work
	$80 \times 80 \times 80$	4.34	0.142	0.150	0.250	0.935	This Work

TABLE 3. Natural convection in a cube. Note: FHKF is Fusegi *et al.* (1991). Ra is the Rayleigh number as defined in FHKF.

Mesh	Re_{cr1}
81×31	1.48×10^3
131×51	1.43×10^3
201×81	1.43×10^3

TABLE 4. Re_{cr1} for $Pr = 6.78$, $A_x = 2.5$ from different meshes.

mesh is used with all variables defined at the cell centre. The pressure-velocity coupling is achieved through solving a Poisson equation for P , Kim & Moin (1985). This Poisson equation is solved using the Jacobi iterative scheme with a V-cycle multigrid procedure. Although the line-by-line Gauss-Seidel sweep converges faster than the Jacobi sweep, the latter is more suitable for vector machines because it provides longer vector length in the multigrid procedure even for the coarsest grid.

Although the use of a non-staggered mesh is known as one source of spurious behaviour of the pressure field in many schemes, no spurious behaviour has been found in our pressure solution, mainly due to strong pressure-velocity coupling in our scheme through accurate satisfaction of mass conservation.

The three-dimensional solver is validated by simulating laminar natural convection in a cube. Fusegi *et al.* (1991) provided a high-resolution finite difference numerical study for cases of $10^3 \leq Ra \leq 10^6$. With Ra larger than 10^4 , they used a $62 \times 62 \times 62$ non-uniform mesh with cells carefully distributed according to the flow pattern. In table 3, results comparison are given at different mesh resolutions. It can be seen that, for $Ra = 10^4$, our solver with uniform mesh of around 24 cells per unit length performs well in predicting average Nusselt number as well as maximum values of u, v and their locations. For the case $Ra = 10^5$, our solver with uniform $32 \times 32 \times 32$ mesh provides excellent results when compared with the much finer $80 \times 80 \times 80$ mesh.

4. Results

4.1. Two-dimensional thermocapillary convection

4.1.1. Mesh dependence checking for Re_{cr} searching

Critical Reynolds numbers are sought using a bisection method until 2 to 3 significant digits in the value of Re_{cr} is obtained. This typically represents 1–3% accuracy in the reported values. Uniform meshes are used in the computations with

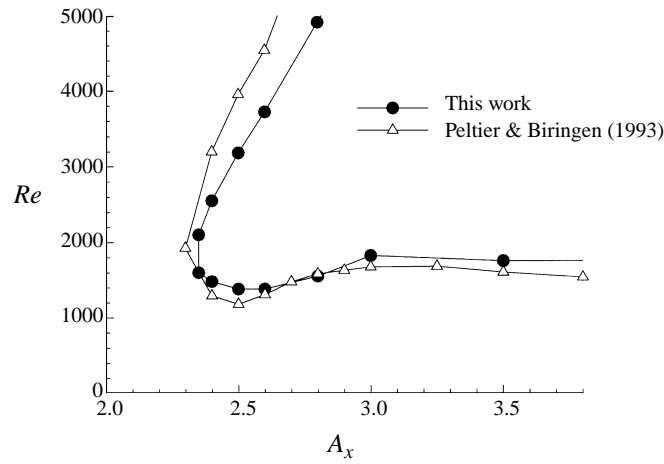


FIGURE 1. Stability diagram for a $Pr = 6.78$ fluid. Good agreement with results by Peltier & Biringen (1993) is obtained.

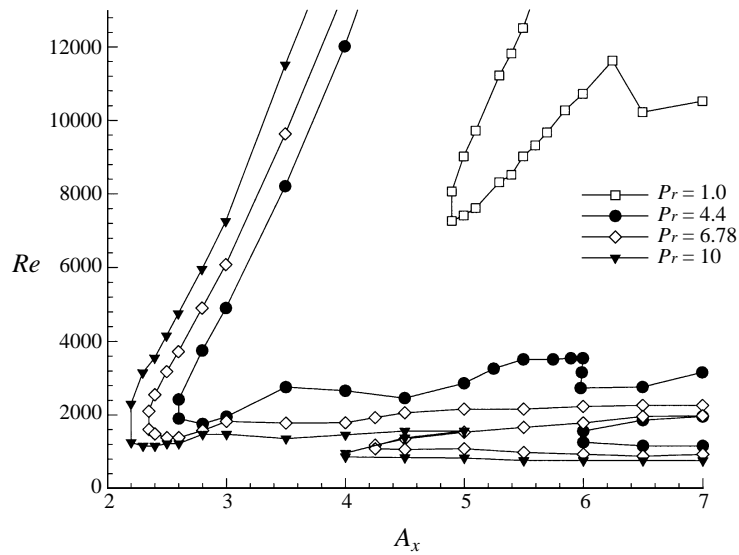


FIGURE 2. Stability diagrams in the (Re, A_x) -plane for fluids with $Pr = 10.0, 6.78, 4.4$ and 1.0 . Multiple regions are present when $Pr \geq 4.4$ and boundaries at different Pr do not intersect.

mesh resolution of 50 to 90 cells per dimensionless unit length depending on the Reynolds number considered. Mesh-dependence of the results is checked at different regions of parameter space. Table 4 gives an example from which it is seen that the mesh resolution with 50 cells per unit length is sufficient for providing almost grid-independent results in searching for critical Reynolds numbers of $O(10^3)$. A coarser mesh with 30 cells per unit length provides results with about 3% difference.

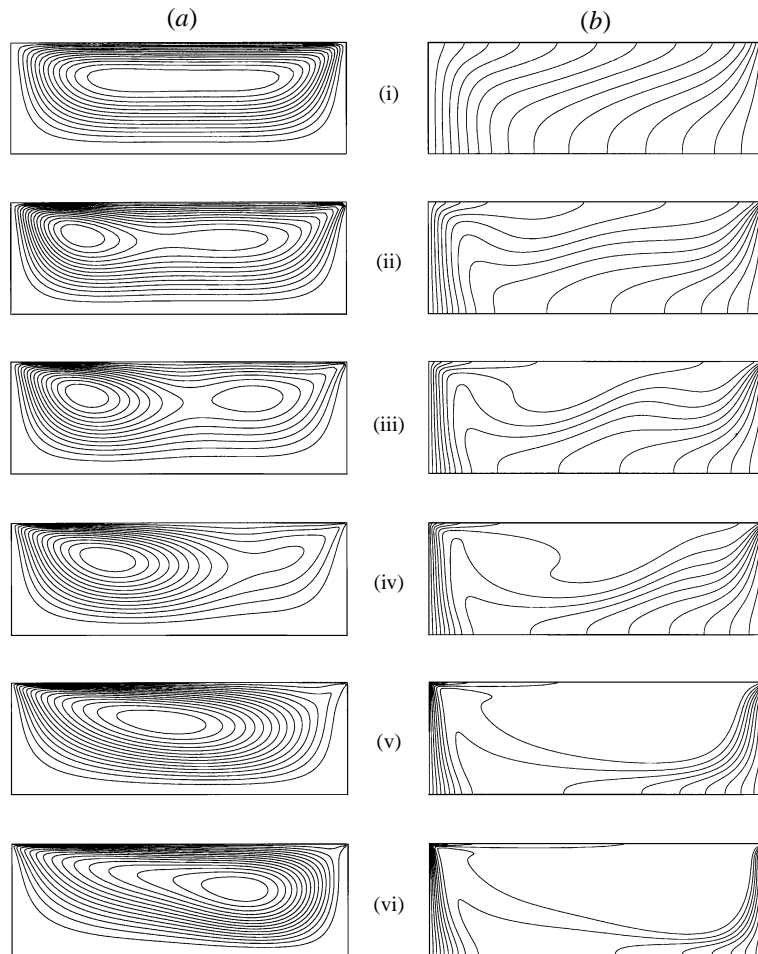


FIGURE 3. Streamline patterns (a) and isotherms (b) for $Pr = 4.4$ flows in an $A_x = 3.0$ cavity at six different Reynolds numbers – 100, 500, 1000, 1950, 5020 and 10 000, (i)–(vi) respectively. Re_{cr1} is about 1950 and Re_{cr2} is about 5020 and mean plots are shown at these values. It is observed that the thermocapillary flow gives rise to an interior that is cooler than the free surface just above. This stratification results in overstability.

4.1.2. Stability diagrams

Peltier & Biringen (1993) considered a $Pr = 6.78$ fluid in rectangular cavities and constructed a stability diagram in the (A_x, Ma) -plane within the range $A_x \leq 3.8$ and $Ma \leq 1.0 \times 10^5$. One of their interesting results is the possible existence of two stability limits at a given A_x . Figure 1 gives a comparison between our stability diagram and their's (the relationship between our Re and their Ma is $Re = Ma/(A_x Pr)$). Good agreement is found and both curves show the existence of a critical aspect ratio ($A_{xcr} \approx 2.3$) below which the flow is stable in the considered range of Reynolds number. In addition, there exists an unstable region bounded by two different critical Reynolds numbers, i.e. as Re goes up, the flow first changes from steady to oscillatory at Re_{cr1} , and then becomes stable again when Re_{cr2} is reached. Re_{cr2} grows monotonically with A_x while Re_{cr1} does not. In the present work, we extend this investigation to fluids with $Pr = 1.0, 4.4$ and 10.0 , and provide stability diagrams for a wider range

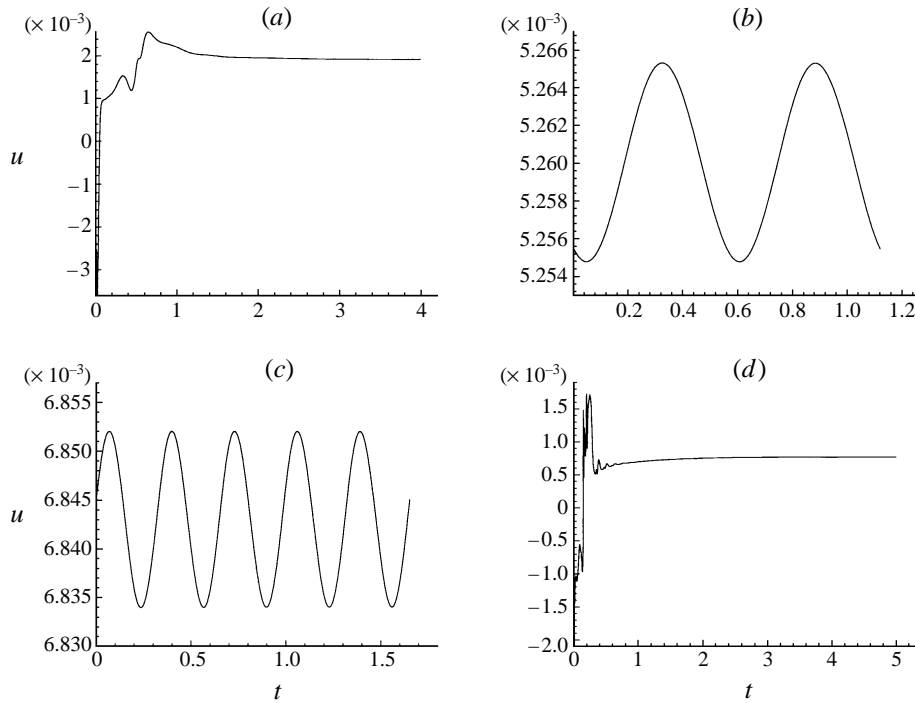


FIGURE 4. Temporal response of u for a point underneath the centre ($X = 1.5$) of the free surface. (a–d) are for $Re = 500, 1950, 5020$ and $10\,000$, respectively, $Pr = 4.4$, and $A_x = 3$. With increasing Re the flow goes through multiple transitions between steady and oscillatory states.

of aspect ratios and Reynolds numbers, in which additional interesting features are found.

Figure 2 is the stability diagram we construct in the (A_x, Re) -plane for fluids with $Pr = 10.0, 6.78, 4.4$ and 1.0 . All curves are within the range $0.0 \leq A_x \leq 7.0$ and $0.0 \leq Re \leq 1.3 \times 10^4$. Several interesting features can be seen from these curves. If we look at the fluid with $Pr = 4.4$ as an example, the first critical aspect ratio is around 2.6. Instability is possible for any $A_x > 2.6$. There is more than one unstable region with $A_x > 6.0$, i.e. if Re increases from zero, the flow is first stable at low Re , starts to oscillate at the first critical point (Re_{cr1}), goes back to stable state at the second critical point (Re_{cr2}), and becomes oscillatory again as Re reaches its third critical point (Re_{cr3}). The existence of the lower limit at (Re_{cr1}) was confirmed in the experiments of Braunsfurth & Homsy (personal communication, 1996) where they observed two-dimensional, multicellular oscillatory states inside our region of instability. In addition, stability curves for fluids with different Pr do not cross each other. Neutral curves of smaller- Pr fluid are always located inside curves of larger Pr , i.e. when Pr becomes smaller, the critical aspect ratio always becomes larger, so does the lowest critical Reynolds number. From the trend given by these curves, one important conclusion that can be drawn is that, for fluids with very low Pr , which are important in material processing of semi-conductors, large values of both critical A_x and Re should be expected for the transition to oscillatory thermocapillary convection. This conclusion is confirmed when we further studied a fluid with $Pr = 0.5$, from which we find a much larger critical aspect ratio of about 10.75 and a Re_{cr1} of about 2.9×10^4 .

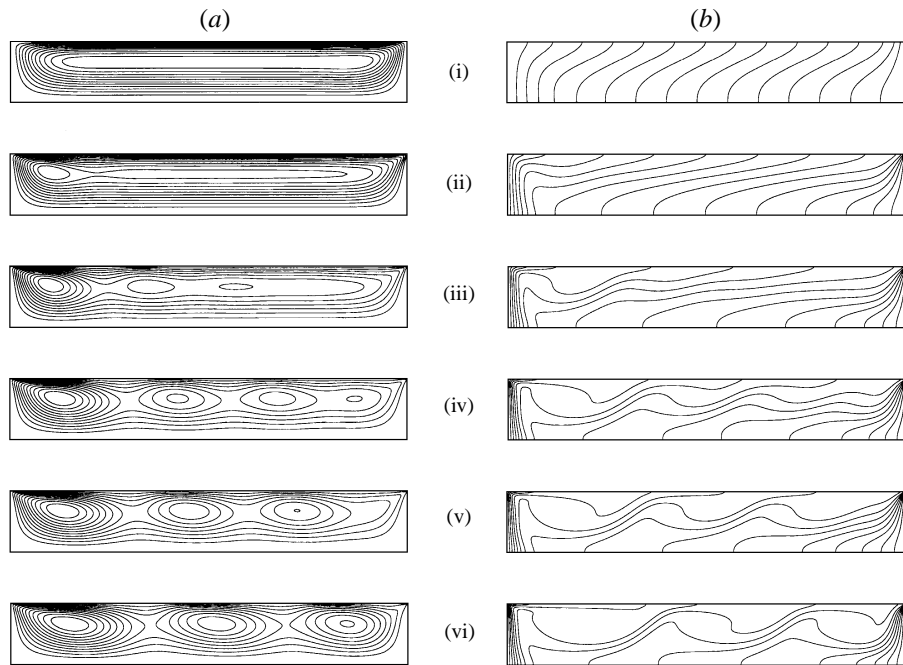


FIGURE 5. Streamlines (a) and isotherms (b) for $Pr = 4.4$ flows in an $A_x = 6.5$ cavity at six different Reynolds numbers – 100, 500, 1170, 1920, 2200 and 2910, (i)–(vi) respectively. Re_{cr1} is about 1170, Re_{cr2} is 1920, and the first critical Re of the higher unstable region is 2910. Thermal stratification similar to that in figure 3 is evident.

4.1.3. Influence of Re and A_x on the flow field with $Pr = 4.4$

At a fixed $A_x = 3$, figure 3 shows the influence of Re on flow structures. When Re is very low, such as $Re = 100$, the flow is steady, temperature gradients do not change much in the whole region, and a single cell structure of streamlines is clearly observed. As Re increases to $Re = 500$ and $Re = 1000$, the flow remains steady – see figure 4(a) for the temporal response; however, the pattern changes to a two-cell structure with a stronger cell near the hot wall, and also, the size of this stronger cell becomes larger when Re is increased from 500 to 1000. Concentration of isotherms can be seen near the hot and cold walls in both figures 3(b) (ii) and 3(b) (iii). Thermal stratification is evident with the interior becoming cooler than the free surface just above. Further increase in Re to the first critical point, which is around 1950, causes the convective flow to oscillate very weakly, with fluctuations of flow quantities being about two orders smaller than the corresponding time averages. The frequency of oscillations near this critical point is about 1.9 – figure 4(b).

That the transition is to an oscillatory state may perhaps be argued as follows. A disturbance that takes a fluid particle from the interior to the free surface simultaneously creates a cold spot due to the thermal stratification just described. Thus surface tension is increased locally pulling surface fluid in and then back into the interior by continuity. Hence the perturbation triggers a restoring mechanism conducive to overstability, and an oscillatory, wave-like state develops.

As mentioned earlier, an interesting feature in the $Pr = 4.4$ stability diagram is the existence of more than one unstable region when $A_x > 6.0$. For example, at $A_x = 6.5$,

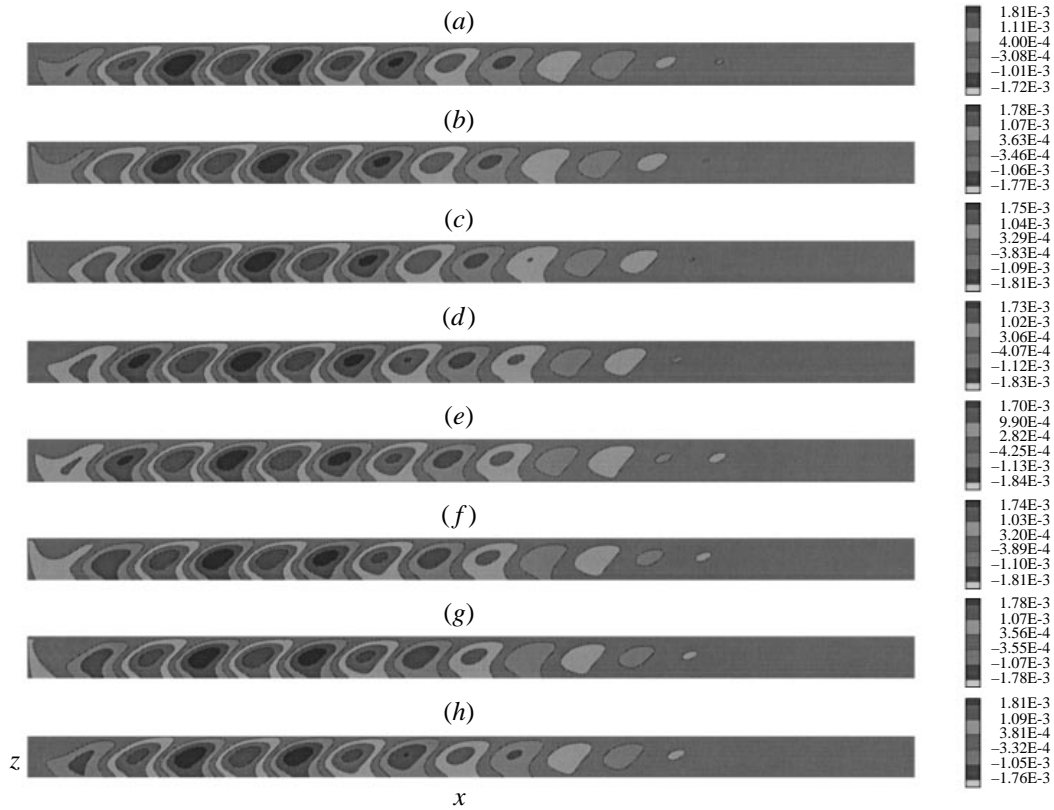


FIGURE 6. Snapshots of temperature disturbances of a $Pr = 10$ fluid in an $A_x = 20$ cavity at eight evenly distributed instances within one oscillation period. Waves travel right to left as predicted by SD. However, in contrast to the infinite layer, not all the cavity participates with the cold corner at steady state.

we find that with increasing Re , the flow starts from stable state, becomes oscillatory for $1170 < Re < 1920$, goes back to stable state for $1920 < Re < 2910$, and oscillates again for $Re > 2910$. Figure 5 shows streamlines and isotherms for six typical points corresponding to $Re = 100, 500, 1170, 1920, 2200$ and 2910 .

For larger aspect ratios such as $A_x = 20$, more cells are expected in the multicellular flow field if Re is big enough. The influence of both the hot and cold walls decreases as the aspect ratio increases. The flow field in the central region of the cavity can be expected to be consistent with that from SD's infinite layer linear stability analysis when Re is smaller or a little higher than its first critical value Re_{cr1} . These expectations are confirmed by our analyses of the $A_x = 20$ case with $Pr = 10$.

4.2. Large aspect ratio case: $A_x = 20$ with $Pr = 10$

Here we look closely at the flow field near the first critical Re , which is about 1012. The oscillation frequency at this Re is about 0.56. A hydrothermal wave propagating toward the left-hand hot wall is evident in figure 6. In an infinite liquid layer, the existence of this wave-like behaviour (nearly two-dimensional for large- Pr fluids), was reported in SD from linear stability of thermocapillary convection. However, a new phenomenon in our results is that this thermal wave seems to be generated

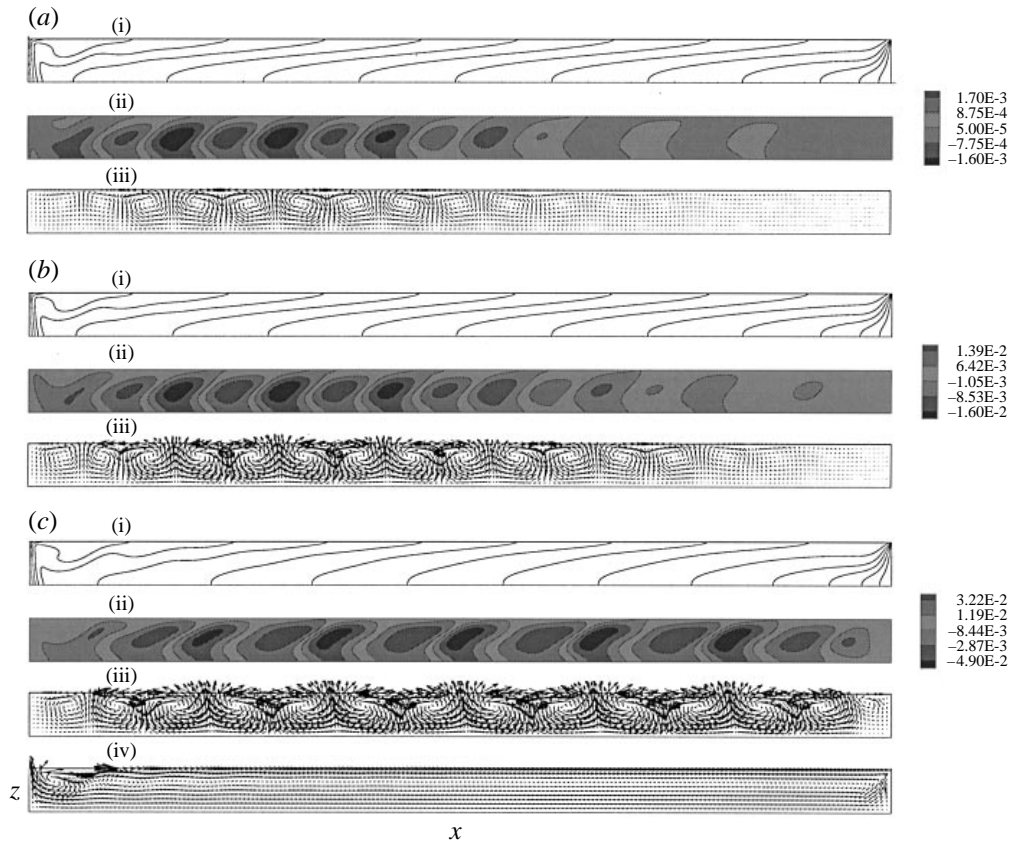


FIGURE 7. (i) Mean temperatures at (a) $Re = 1012$, (b) 1023 and (c) 1500 , respectively, with $Pr = 10$ and $A_x = 20$. (ii) Snapshots of corresponding temperature fluctuations, and (iii) velocity fluctuations at the same Re as (i). (iv) The mean velocity field at $Re = 1500$. While all the waves are supercritical, they fill the cavity and begin at the cold corner only at the highest Re .

near the centre of the cavity, and most of the region in the right-hand part of the cavity, close to the cold surface, remains pretty calm. The starting point of the thermal wave actually moves toward the cold wall as we increase Re , until it occupies the whole cavity. This trend is obvious from figures 7(a) (ii), 7(b) (ii) and 7(c) (ii). Velocity fluctuations are given in figures 7(a) (iii), 7(b) (iii) and 7(c) (iii), from which one can see the existence of multi-cellular flow structures. The last picture, figure 7(c) (iv), is the mean velocity field corresponding to $Re = 1500$. A strong cell structure can be seen in the region close to the hot wall, which is very similar to the structure we saw in previous results for $A_x = 6.5$. Indeed, the structure of the mean field is qualitatively almost the same for all three cases of $Re = 1012$, 1023 and 1500 .

For $Re = 1012$, the mean temperature distribution on the free surface is given in figure 8(a). It can be seen that the temperature variation in the central region is almost linear with slope $dT/dx = 0.028$. Based on this slope, the critical Marangoni number Ma_c , consistent with the definition for linear analysis, is about 283 which matches very well with about 300 from SD. The difference is probably due to our model which is both two-dimensional and with finite A_x . Figure 8(b) is a plot of the

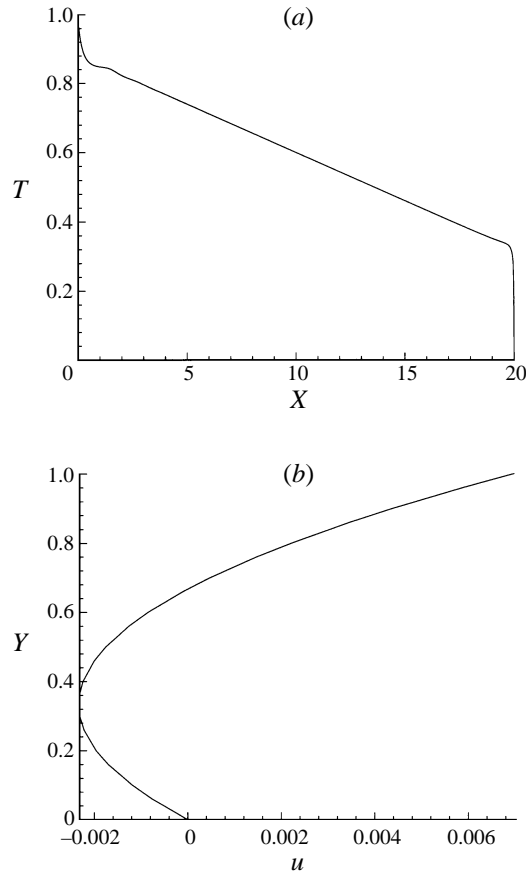


FIGURE 8. Variation of mean temperature on the free surface and mean velocity u at the centerline $x = 10$ for the case of $Re = 1012, Pr = 10$ and $A_x = 20$. This is essentially the return flow of SD with the Marangoni number based on the straight line segment in (a).

mean velocity component U along the y -axis in the central region of the cavity which is essentially the return flow of SD.

4.3. Two-dimensional energy analysis with $A_x = 3$ and $Pr = 10$

Here we report on energy analyses of flows with Reynolds numbers near both the lower ($Re = 1540$) and higher ($Re = 7410$) critical points of the unstable region. Temporal variations over one oscillation period are shown in figures 9(a) (i) and 9(a) (ii) for the rate of change of the total fluctuation kinetic energy ($dK/d\tau$) as well as its components I_{k_1} (production), I_{k_2} (diffusion) and I_{k_3} (dissipation). It is seen that $dK/d\tau$ oscillates with its time average being equal to zero, which means no kinetic energy is added to the flow over each period of oscillation. This is consistent with the fact that the flow field oscillates at a stable amplitude. I_{k_2} and I_{k_3} provide major contributions with I_{k_2} being always positive (destabilizing) and I_{k_3} being always negative (stabilizing). Both the time average and oscillating magnitudes of I_{k_1} are much smaller than those of I_{k_2} and I_{k_3} , which indicate that the flow is strongly viscous. However, the phase difference between I_{k_2} and I_{k_3} is always near π , thus I_{k_3} always balances the effect of I_{k_2} , and therefore the smaller term I_{k_1} still has an

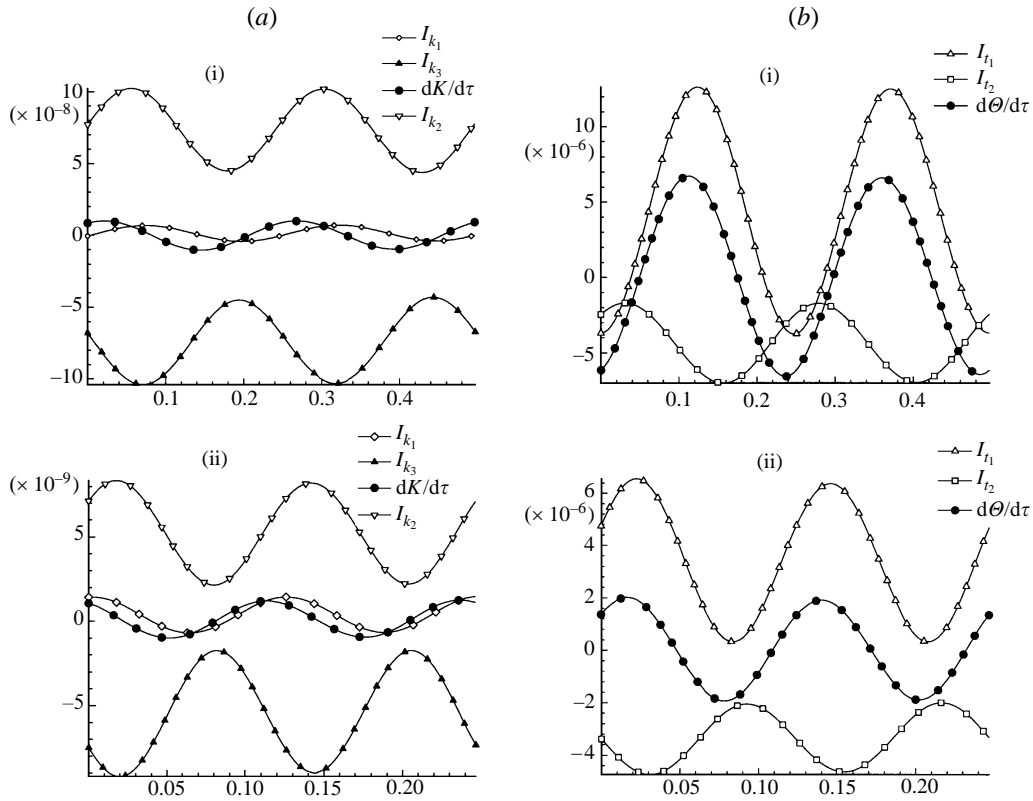


FIGURE 9. Temporal variation of the rate of change of the total kinetic energy $dK/d\tau$, the thermal energy $d\Theta/d\tau$ and their components I_{k_1} , I_{k_2} , I_{k_3} , I_{t_1} and I_{t_2} , in which (a) (i) and (b) (i) give results for $Re = 1540$ (near the lower critical point), (a) (ii) and (b) (ii) provide results for $Re = 7410$ (near the higher critical point). In the text it is argued that I_{t_1} provides the mechanism for instability.

apparent strong influence on the temporal behaviour of $dK/d\tau$. In figure 9(a) (ii), which is at the higher critical point, one can clearly see that $dK/d\tau$ oscillates at a very close amplitude and a very small phase difference with I_{k_1} , while the phase difference between I_{k_2} and I_{k_3} is almost π .

Results for thermal energy fluctuations ($d\Theta/d\tau$) and its components (I_{t_1} and I_{t_2}) are given in figures 9(b) (i) and 9(b) (ii) for the lower and higher critical points, respectively. As expected, $d\Theta/d\tau$ oscillates with its time average being equal to zero, since the temperature field also oscillates in a limit cycle. Although the time averages of I_{t_1} and I_{t_2} have the same absolute value, the oscillation amplitude of I_{t_1} is much larger than that of I_{t_2} . Furthermore, in both cases, the phase difference between I_{t_1} and $d\Theta/d\tau$ is very small. It may thus be argued that I_{t_1} , which is the rate of transfer of thermal energy from the gradient of the mean field by the fluctuations velocity to thermal disturbance, is the mechanism responsible for loss of stability. This mechanism was also identified in Wanschura *et al.* (1995) as the high- Pr instability mechanism. This conclusion is also consistent with the unstable thermal stratification of the mean temperature fields described earlier.

We also investigated the spatial variations of the rate of change of both the kinetic energy ($Dk/D\tau$) given by (15), and the thermal energy ($D\theta/D\tau$) given by (20) over

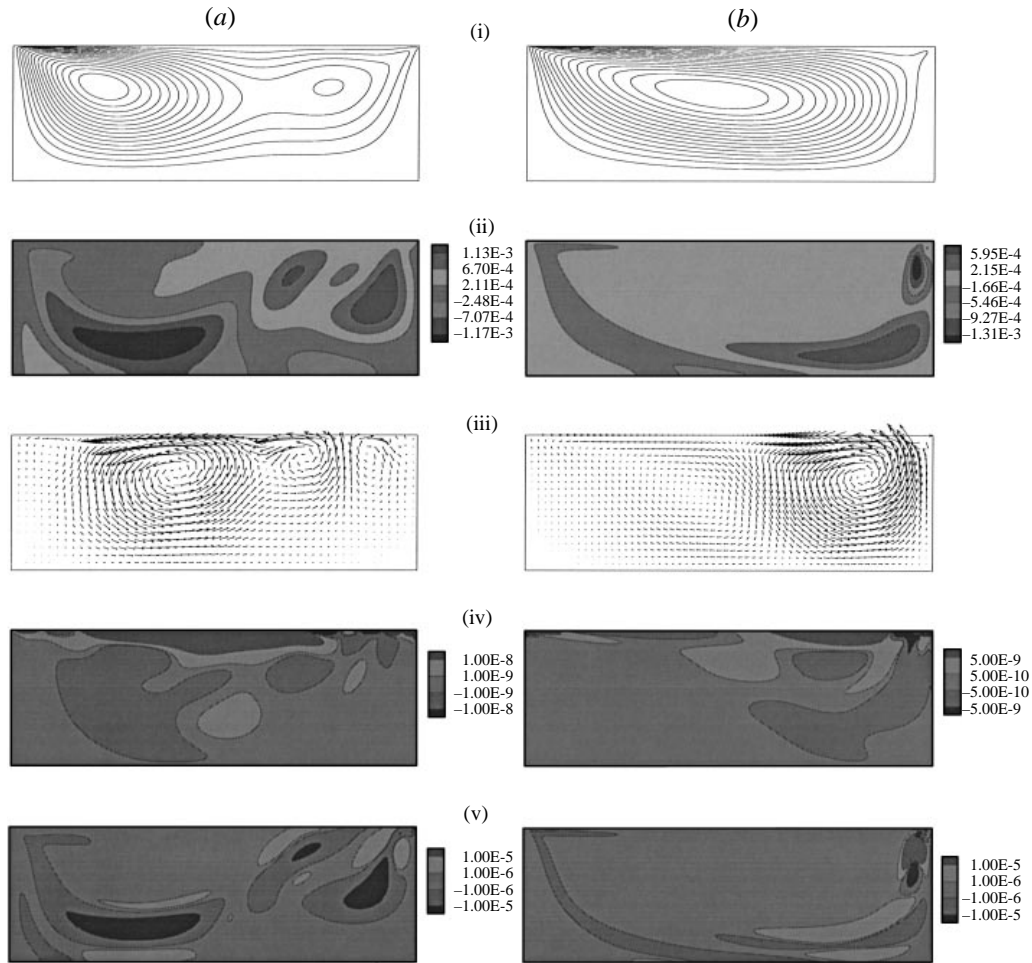


FIGURE 10. Results of energy calculations with $Pr = 10$ and $A_x = 3$. (a) Mean flow, snapshots (at $\tau = 0$ of figure 9) of temperature, velocity, kinetic energy, and thermal energy fluctuations, (i)–(v) respectively at $Re = 1540$. (b) Corresponding plots at $Re = 7410$. Strong sources and sinks for kinetic energy locate near the free surface while those for thermal energy penetrate in the interior in a manner dictated by the flow patterns in (i).

the whole domain at different time instants during one oscillation period. At the instant corresponding to $\tau = 0$ in figure 9, results are provided for $Re = 1540$ (near Re_{cr1}) and 7410 (near Re_{cr2}) in figure 10 where it can be seen that most of the strong sources and sinks of the fluctuation kinetic energy are located near the free surface. This appears to be consistent with the location of the only driving force for thermocapillary convection.

4.4. Three-dimensional studies

The influence of front and back sidewalls and possible motion in the third direction have been neglected in two-dimensional studies. The purpose of the present three-dimensional work is to find out their effects on flow instability.

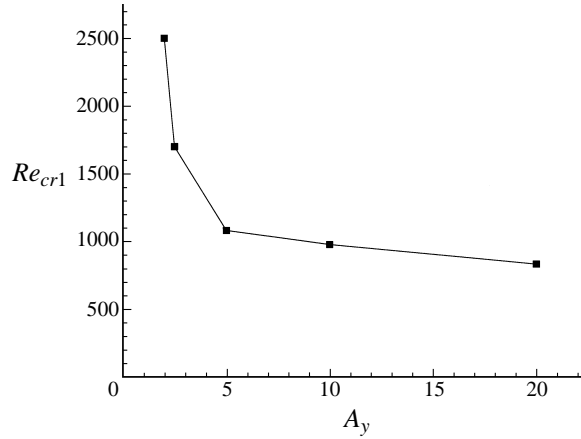


FIGURE 11. Variation of Re_{cr1} as A_y changes from 2 to 20 with $Pr = 4.4$ and $A_x = 3$. Damping effects are evident with $A_y \leq 5$.

4.4.1. Cavities with $A_x = 3$ and varying A_y

Intuitively, the front and back sidewalls are expected to suppress oscillations so that when the cavity width aspect ratio A_y is small the first critical Reynolds number (Re_{cr1}) should be larger than its two-dimensional counterpart.

The first investigation is for a $Pr = 4.4$ fluid with fixed $A_x = 3$ and different values of A_y . Attention is focused on changes of Re_{cr1} as A_y varies from 20 down to 2.0. The neutral curve in figure 11, obtained in similar way as in two dimensions, shows that Re_{cr1} changes slowly from around 850 at $A_y = 20$ to around 1100 at $A_y = 5$. However, it goes up very fast as A_y becomes smaller than 5. Another interesting observation is that when A_y is large, i.e. the influence of the sidewalls is small, Re_{cr1} goes below 1000, which is much smaller than the corresponding value of $Re_{cr1} = 1950$ for the same value of $Pr = 4.4$ and $A_x = 3.0$ in two-dimensional analysis. This suggests that there must be some other three-dimensional mechanism strongly affecting flow instability when $Pr = 4.4$ in a cavity with $A_x = 3.0$. This three-dimensional mechanism is found to be the initiation of spanwise waves somewhat similar to the longitudinal two-dimensional hydrothermal waves of SD.

Figure 12 shows snapshots corresponding to four instants of the temperature perturbations on the free surface in a half oscillation period with $Re = 850$ and $A_y = 20$. The other half of the period is omitted since every two instants with phase difference of π have the same isotherm pattern with an opposite sign. Symmetry with respect to the plane $y = 10$ is exhibited in these plots. In the central region the isotherms form a number of cellular structures, moving from right to the left in the x -direction. However, waves are triggered in the y -direction. This, we believe, is the reason why we have instability at Re lower than the two-dimensional critical value of 1950. We do not attempt quantitative comparisons with SD's longitudinal waves since they are triggered by a return flow which is not available in our cavity with $A_x = 3$.

Similar calculations are also done at the larger $Pr = 13.9$ in a cavity with $A_x = 3$ and $A_y = 20$. Re_{cr1} is found to be about 1000, which is a little higher than the corresponding two-dimensional $Re_{cr1} = 770$. The reason for the different three-dimensional influence on Re_{cr1} with $Pr = 4.4$ and $Pr = 13.9$ is obtained from examination of free-surface

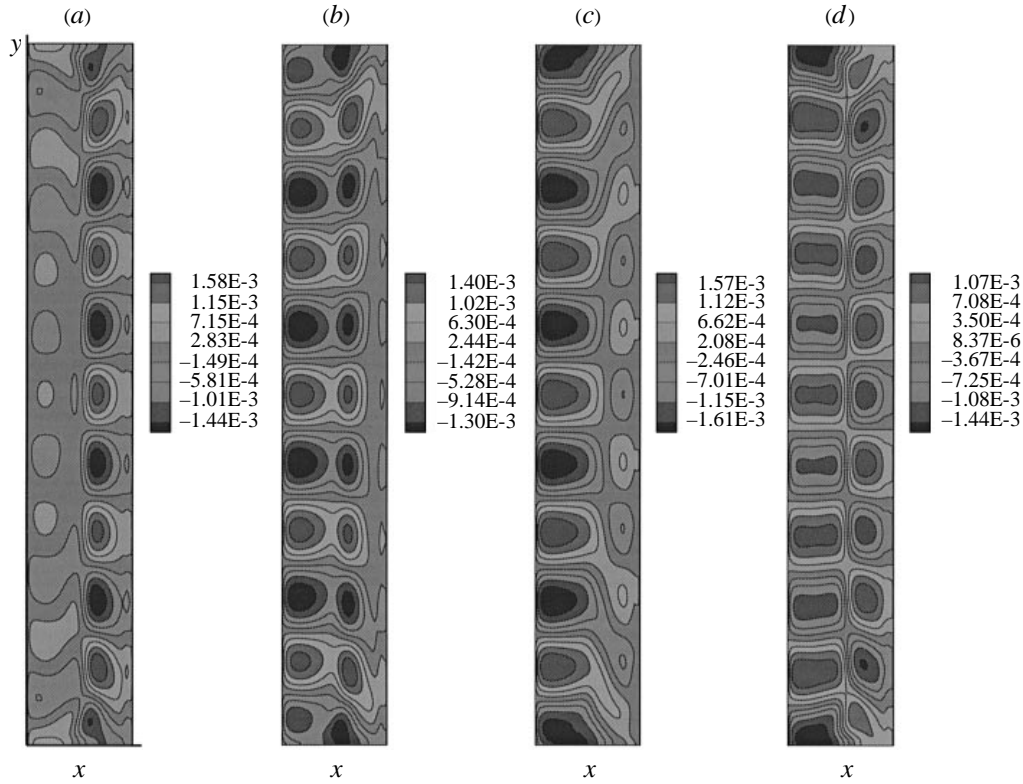


FIGURE 12. Snapshots of temperature fluctuations on the free surface of a $3 \times 20 \times 1$ cavity with a $Pr = 4.4$ fluid at $Re = 850$ at four instances at $T/8$, $T/4$, $3T/8$ and $T/2$, (a)–(d) respectively (T is the period of oscillations). Spanwise waves are also triggered at this Re and are symmetric with respect to $y = 10$.

plots. Mean temperature fields are given in figure 13(a) (i) and 13(b) (i) from which one can find that isotherms are parallel in the central region for both cases. However, the fluctuation temperature field with $Pr = 4.4$ in (a) (ii) are totally different from that with $Pr = 13.9$ in (b) (ii): there is no periodic structure in the y -direction for the $Pr = 13.9$ case. It is also observed that the magnitude of fluctuations of v in (a) (iv) is slightly larger than that of u in (a) (iii) for the case of $Pr = 4.4$, while fluctuations of u in (b) (iii) are more than one order of magnitude larger than that of v in (b) (iv) for the case of $Pr = 13.9$. Thus, with $Pr = 13.9$, the streamwise fluctuations are dominant and the spanwise fluctuations are too weak. Re of 1000 is simply not high enough to trigger spanwise waves. This is consistent with the fact that the critical Marangoni number of the two-dimensional longitudinal waves of SD increases with Pr . On the contrary, with $Pr = 4.4$, spanwise fluctuations are very strong, even stronger than the streamwise fluctuations, which explains why Re_{cr1} is overestimated in two-dimensional calculations when the only motion allowed is streamwise.

4.4.2. A $Pr = 13.9$ fluid in a cavity with $A_x = A_y = 15$

Here Re_{cr1} is found to be around 700 and the oscillation frequency is about 0.5. On the free surface, in the region not too close to sidewalls at $y = 0$ and $y = 15$, the mean

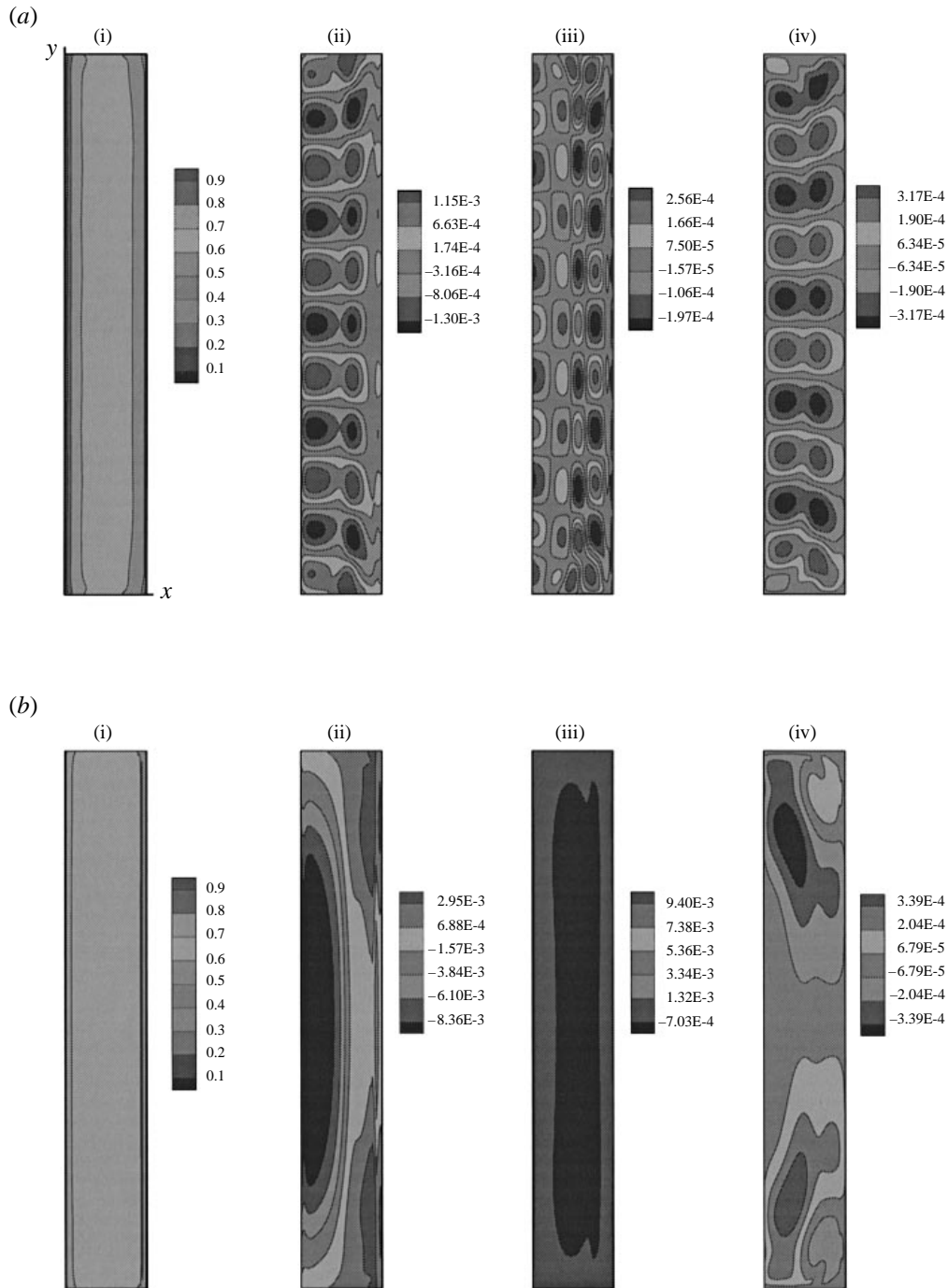


FIGURE 13. Comparison of free surface flows in a $3 \times 20 \times 1$ cavity. (a) $Pr = 4.4$ and $Re = 850$ showing mean temperature distribution, snapshots of the fluctuations t , u and v , (i)–(iv) respectively. (b) Corresponding snapshots for a $Pr = 13.9$ fluid at $Re = 1000$. Spanwise oscillations in (a) occur at Re which is lower than the two-dimensional critical value of about 1950. In (b) sidewalls continue to have a damping effect with an increased critical Re compared to the two-dimensional value of 770.

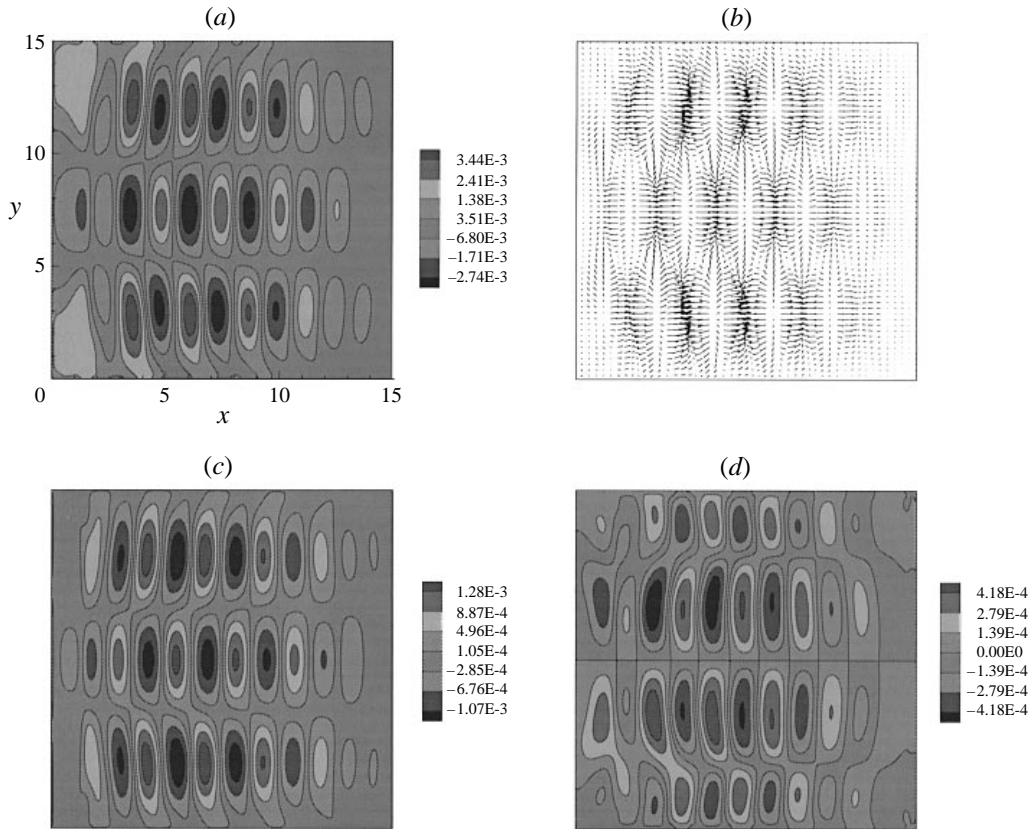


FIGURE 14. Free surface results for the case of a $Pr = 13.9$ fluid in a $15 \times 15 \times 1$ cavity at $Re = 710$. (a) A snapshot of fluctuation isotherms, (b) of fluctuation velocity vector field, (c) and (d) are contours of fluctuation velocity components u and v , respectively. Phase lines inclined at angles of about $\pm 15^\circ$ to the y -axis are evident and are in good agreement with SD's linear stability results.

temperature distribution along the streamwise direction is qualitatively very similar to that shown in figure 8(a). It also has a linear central region but with $dT/dx = 0.032$. Based on this slope, the critical Marangoni number corresponding to the definition in SD is about 311 which is very close to their value of 295. The difference can be attributed to the damping effect of the sidewalls.

In figure 14(a) a snapshot of temperature perturbations on the free surface is given, in which one can see the existence of a multi-cellular structure symmetric with respect to the central plane $y = 7.5$. The aspect ratio of these cells is about 1:3.8 which gives a wave-front inclination angle of about 15° with respect to the y -axis. This is in good agreement with about 20° from linear theory. Figure 14(b) gives a snapshot of the fluctuating velocity vector field, while (c) and (d) are contour plots for the u and v components, respectively. The fluctuations u are about three times larger than v , indicating again that streamwise perturbations are much stronger than spanwise perturbations for larger Pr . Figure 15(a) (i) is the mean temperature field in the $x = 7.5$ plane from which one can see the influence of the front and back sidewalls is restricted to near-wall regions and hence isotherms in most of the central region are parallel. Figures 15(a) (ii) and 15(a) (iii) show three-cell structures for the

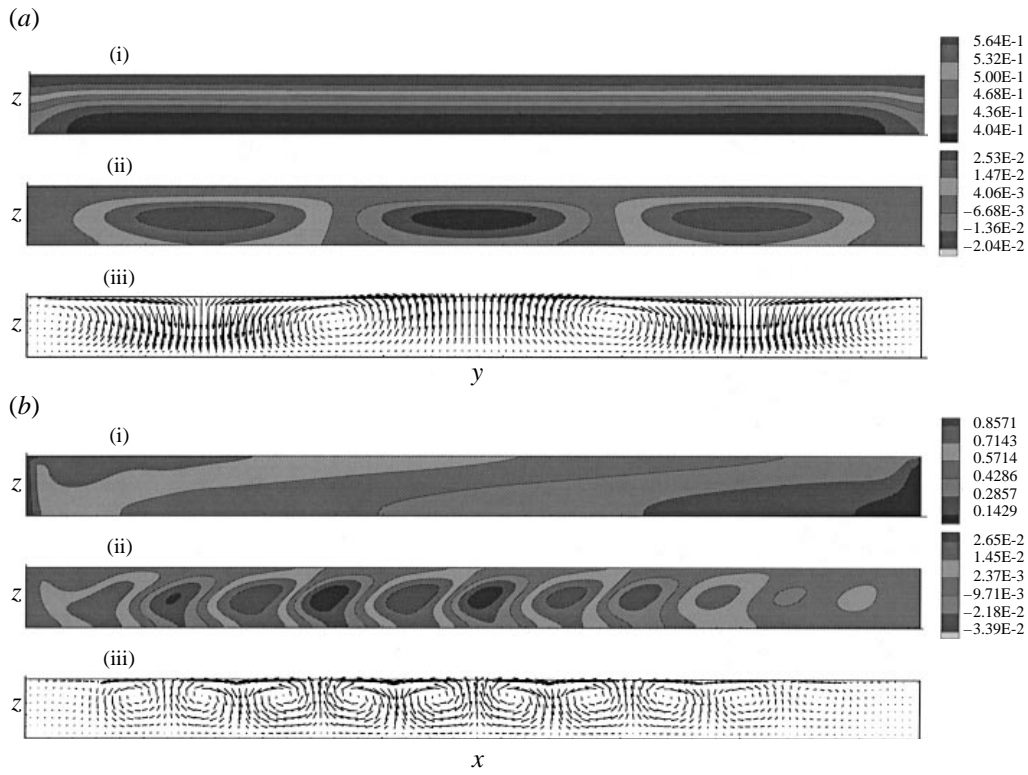


FIGURE 15. Motion in a $15 \times 15 \times 1$ cavity with $Pr = 13.9$ and $Re = 710$. (a) Plane $x = 7.5$ and gives (i) mean temperature distribution, (ii) and (iii) provide snapshots of fluctuation temperature distribution and fluctuation velocity field, respectively. (b) Corresponding pictures in the plane $y = 7.5$. Sidewalls have weak effects in most of the cavity with the x -motion in mid-cavity very similar to that in the long two-dimensional cavity of figure 7.

temperature and velocity disturbance fields. Finally, from figures 15(b) (i), 15(b) (ii) and 15(b) (iii), one finds structures of temperature perturbation and corresponding velocity perturbation in the plane of $y = 7.5$ that are qualitatively very similar to those in figure 7 corresponding to two-dimensional waves with $A_x = 20$ and $Pr = 10$. We thus have travelling x -waves and standing y -waves which can be thought of as a superposition of two hydrothermal waves propagating in the negative x -direction at $\pm 15^\circ$ with respect to y .

5. Conclusions

Two- and three-dimensional thermocapillary-driven convection is investigated primarily to determine its stability characteristics. In two dimensions, neutral curves are delineated in the (Re, A_x) -plane for fluids with $Pr = 1.0, 4.4, 6.78$ and 10 . Interesting features are discussed, including the existence of multi-unstable regions when $Pr \geq 4.4$. Results are also provided to show the influence of Re and A_x on flow structure. Energy analyses are performed on oscillatory flows with Re very close to critical points. The roles of production, diffusion, and dissipation components of fluctuation kinetic and thermal energies are discussed, and the mechanisms responsible for transition to oscillatory states are pointed out.

In three dimensions, the influence of front and back sidewalls as well as spanwise fluctuations on transition was determined. With $Pr = 4.4$ and $A_x = 3$, these walls have weak effect when A_y is greater than 5, and they severely suppress oscillations when A_y is less than 3. However, at large A_y such as 20, due to the existence of spanwise fluctuations, transition occurs at a much lower Re than that required by pure streamwise instability. With a larger Pr of 13.9, sidewalls have a damping effect even with $A_y = 20$. Direct numerical simulations of waves in a cavity with large A_x and A_y were also performed. The waves observed near the first critical Reynolds number are in good agreement with those predicted by linear stability of an infinite layer.

This research is sponsored by NASA through grant No. NAG3-1453. We also acknowledge the Pittsburgh Supercomputing Center for providing CRAY C90 time through grants No. CTS950032P, CTS960014P and CTS960032P.

REFERENCES

- BEN HADID, H. & ROUX, B. 1990 Thermocapillary convection in long horizontal layers of low-Prandtl-number melts subject to horizontal temperature gradient. *J. Fluid Mech.* **221**, 77–103.
- BIRIKH, R. V. 1966 Thermocapillary convection in horizontal layer of liquid. *J. Appl. Mech. Texh. Phys.* **7**, 43–49.
- BRAUNSFURTH, M. G. & HOMSY, G. M. 1997 Combined thermocapillary-buoyancy convection in a cavity. Part II. An experimental study. *Phys. Fluids* **9**, 1277–1286.
- CARPENTER B. M. & HOMSY, G. M. 1989 High Marangoni number convection in a square cavity: Part II. *Phys. Fluids A* **2**, 137–149.
- CHUN, C. H. 1980 Experiments on the transition from the steady to the oscillatory temperature distribution in a floating zone due to Marangoni convection. *Acta Astronautica* **7**, 479–488.
- CHUN, C. H. & WUEST, W. 1979 Experiments on the transition from the steady to the oscillatory Marangoni convection of a floating zone under reduced gravity effect. *Acta Astronautica* **6**, 1073–1082.
- DAVIAUD, F. & VINCE, J. M. 1993 Traveling waves in a fluid layer subjected to a horizontal temperature gradient. *Phys. Rev. E* **8**, 443–4436.
- DAVIS, S. H. 1987 Thermocapillary instabilities. *Ann. Rev. Fluid Mech.* **19**, 403–435.
- DE SAEDELEER, C., GARCIMARTIN, A., CHAVEPEYER, G. & PLATTEN, J. K. 1996 The instability of a liquid layer heated from the side when the upper surface is open to air. *Phys. Fluids* **8**, 670–676.
- FUSEGI, T., HYUN, J. M., KUWAHARA, K. & FAROUK, B. 1991 A numerical study of three-dimensional natural convection in a differentially heated cubical enclosure. *Intl J. Mass Transfer* **34**, 1543–1557.
- HURLE, D. T. J. 1967 Thermo-hydrodynamic oscillation in liquid metals: the cause of impurities striations in melt-grown crystals. *J. Phys. Chem. Solids* **1**, 659–669.
- JANSSEN, R. J. A. & HENKES, R. A. W. M. 1995 Influence of Prandtl number on instability mechanisms and transition in a differentially heated square cavity. *J. Fluid Mech.* **290**, 319–344.
- KAMOTANI, Y., OSTRACH, S. & VARGAS, M. 1984 Oscillatory thermocapillary convection in a simulated floating zone configuration. *J. Crystal Growth* **66**, 83–90.
- KIM, J. & MOIN, P. 1985 Application of a fractional-step method to incompressible Navier-Stokes equations. *J. Comput. Phys.* **59**, 308–323.
- LEVENSTAM, M. & AMBERG, G. 1995 Hydrodynamical instabilities of thermocapillary flow in a half-zone. *J. Fluid Mech.* **297**, 357–372.
- LEVICH, H. G. & KRYLOV, V. S. 1969 Surface tension-driven phenomena. *Ann. Rev. Fluid Mech.* **1**, 293–316.
- MÜLLER, G. 1988 Convection and inhomogeneities in crystal growth from the melt. *Crystals, Properties, and Applications*, Vol. 12. Springer.
- OSTRACH, S. 1982 Low-gravity fluid flows. *Ann. Rev. Fluid Mech.* **14**, 313–345.

- PELTIER, L. J. & BIRINGEN, S. 1993 Time-dependent thermocapillary convection in a rectangular cavity: numerical results for a moderate Prandtl number fluid. *J. Fluid Mech.* **257**, 339–357.
- PREISSER, F., SCHWABE, D. & SCHARMANN, A. 1983 Steady and oscillatory thermocapillary convection in liquid columns with free cylindrical surface. *J. Fluid Mech.* **126**, 545–567.
- RILEY, R. J. & NEITZEL, G. P. 1998 Instability of thermocapillary-buoyancy convection in shallow layers. Part 1. Characterization of steady and oscillatory instabilities. *J. Fluid Mech.* **359**, 143–164.
- ROUX, B. 1990 *Numerical Simulation of Oscillatory Convection in Low-Pr Fluids - A GAMM Workshop*. Notes on Numerical Fluid Mechanics, Vol. 27. Vieweg Braunschweig.
- SAB, V., KUHLMANN, H. C. & RATH, H. J. 1996 Investigation of three-dimensional thermocapillary convection in a cubic container by a multi-grid method. *Intl J. Heat Mass Transfer* **39**, 603–613.
- SMITH, M. K. 1986 Instability mechanisms in dynamic thermocapillary liquid layers. *Phys. Fluids* **29**, 3182–3186.
- SMITH, M. K. & DAVIS, S. H. 1983 Instabilities of dynamic thermocapillary liquid layers. Part 1. Convective instabilities. *J. Fluid Mech.* **132**, 119–144 (referred to herein as SD).
- STRANI, M., PIVA, R. & GRAZIANI, G. 1983 Thermocapillary convection in a rectangular cavity: asymptotic theory and numerical simulation. *J. Fluid Mech.* **130**, 347–376.
- VELTEN, R., SCHWABE, D. & SCHARMANN, A. 1991 The periodic instability of thermocapillary convection in cylindrical liquid bridges. *Phys. Fluids A* **3**, 267.
- WANSCHURA, M., SHEVTSOVA, V. M., KUHLMANN, H. C. & RATH, H. J. 1995 Convective instability mechanisms in thermocapillary liquid bridges. *Phys. Fluids* **7**, 912–925.
- WILKE, H. & LÖSER, W. 1983 Numerical calculation of Marangoni convection in a rectangular open boat. *Cryst. Res. Technol.* **6**, 825–833.
- XU, J. 1997 Stability analysis of two- and three-dimensional thermocapillary convection. PhD Dissertation, Rutgers University.
- YIH, C. S. 1968 Fluid Motion induced by surface-tension variation. *Phys. Fluids* **3**, 477–480.
- ZEBIB, A., HOMSY, G. M. & MEIBURG, E. 1985 High Marangoni number convection in a square cavity. *Phys. Fluids* **28**, 3467–3476.